UC Irvine
UC Irvine Previously Published Works

Title

Driving Chemical Reactions in Plasmonic Nanogaps with Electrohydrodynamic Flow.

Permalink

https://escholarship.org/uc/item/15b196kh

Journal

ACS nano, 11(11)

ISSN

1936-0851

Authors

Thrift, William J
Nguyen, Cuong Q
Darvishzadeh-Varcheie, Mahsa
et al.

Publication Date

2017-11-01

DOI

10.1021/acsnano.7b05815

Peer reviewed

Driving Chemical Reactions in Plasmonic Nanogaps with Electrohydrodynamic Flow

William J. Thrift,[†] Cuong Q. Nguyen,[†] Mahsa Darvishzadeh-Varcheie,[‡] Siavash Zare,[§] Nicholas Sharac,[∥] Robert N. Sanderson,[⊥] Torin J. Dupper,[∥] Allon I. Hochbaum,[†,∥] Filippo Capolino,[‡] Mohammad Javad Abdolhosseini Qomi,[§] and Regina Ragan[*,†]

[†]Department of Chemical Engineering and Materials Science, University of California, Irvine, Irvine, California 92697-2575, United States

[‡]Department of Electrical Engineering and Computer Science, University of California, Irvine, Irvine, California 92697-2625, United States

[§]Department of Civil and Environmental Engineering, University of California, Irvine, Irvine, California 92697-2175, United States

[∥]Department of Chemistry, University of California, Irvine, Irvine, California 92697-2025, United States

[⊥]Department of Physics and Astronomy, University of California, Irvine, Irvine, California 92697-4575, United States

S Supporting Information

ABSTRACT: Nanoparticles from colloidal solution—with controlled composition, size, and shape—serve as excellent building blocks for plasmonic devices and metasurfaces. However, understanding hierarchical driving forces affecting the geometry of oligomers and interparticle gap spacings is still needed to fabricate high-density architectures over large areas. Here, electrohydrodynamic (EHD) flow is used as a long-range driving force to enable carbodiimide cross-linking between nanospheres and produces oligomers exhibiting sub-nanometer gap spacing over mm² areas. Anhydride linkers between nanospheres are observed *via* surface-enhanced Raman scattering (SERS) spectroscopy. The anhydride linkers are cleavable *via* nucleophilic substitution and enable placement of nucleophilic molecules in electromagnetic hotspots. Atomistic simulations elucidate that the transient attractive force provided by EHD flow is needed to provide a sufficient residence time for anhydride cross-linking to overcome slow reaction kinetics.

This synergistic analysis shows assembly involves an interplay between long-range driving forces increasing nanoparticle–nanoparticle interactions and probability that ligands are in proximity to overcome activation energy barriers associated with short-range chemical reactions. Absorption spectroscopy and electromagnetic full-wave simulations show that variations in nanogap spacing have a greater influence on optical response than variations in close-packed oligomer geometry. The EHD flow–anhydride cross-linking assembly method enables close-packed oligomers with uniform gap spacings that produce uniform SERS enhancement factors. These results demonstrate the efficacy of colloidal driving forces to selectively enable chemical reactions leading to future assembly platforms for large-area nanodevices.

KEYWORDS: *plasmonics, electrohydrodynamic flow, colloidal assembly, chemical cross-linking, reactive molecular dynamics, rare event, minimum energy path*
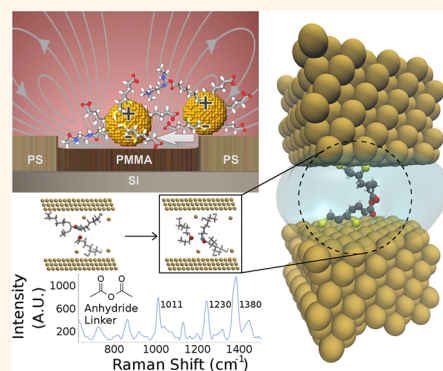
Since seminal reports demonstrating assembly of super-lattices from colloidal dispersions were published,[1] the fundamental understanding of material, geometric tolerances, and process parameters in the assembly of nanospheres from colloids has led to long-range order in superlattice thin films on the wafer scale,[2,3] marking significant progress in the ability to structure matter from molecular to mesoscopic length scales. In the case of 2D plasmonics and metasurfaces, it is often desirable to fabricate discrete assemblies rather than closed-packed films, and this requires further understanding of hierarchical driving forces (long-range

and short-range) for control of resultant architectures.[4] These discrete assemblies are often referred to as oligomers because plasmon hybridization theory intuitively describes the electromagnetic response using an analogy with molecular orbital theory.[5] Nanoparticle colloids thus provide metamolecule building blocks where not only composition, size, and shape of the nanoparticle but the geometry of resultant oligomers, gap
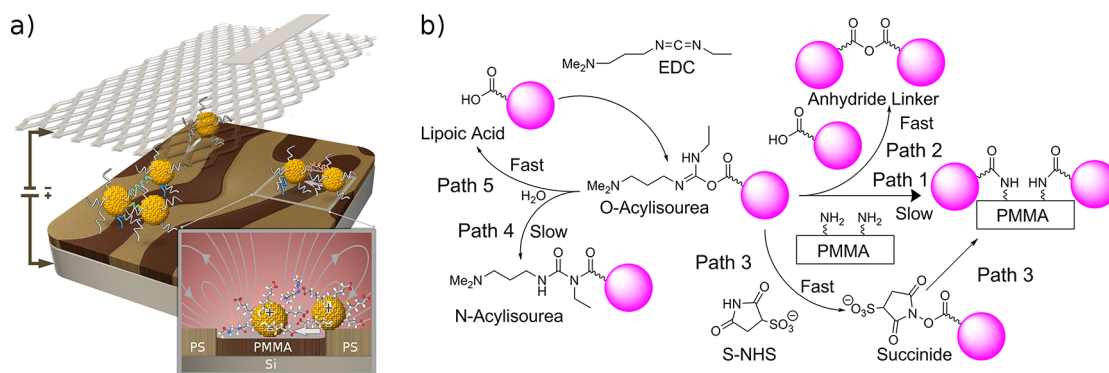
Figure 1. (a) Schematic of EHD attractive forces in a colloidal solution of carboxylic acid-functionalized Au nanospheres near the working electrode composed of a self-organized PS-*b*-PMMA diblock copolymer template on Si. The inset depicts the EHD flow that entrains nearby particles around a Au seed, increasing the probability of nanosphere−nanosphere collisions. (b) Carbodiimide chemistry pathways yield covalent linkages to the amine-functionalized surface *via* paths 1 and 3, while covalent linkages between nanospheres are achieved through path 2.

spacings, and dielectric environment provide additional degrees of freedom for tuning the electromagnetic response.[6−9] Our early work has demonstrated that metal nanoparticles from colloids can be assembled in oligomers over large areas using self-organized chemical patterns[10] that produce enhanced electromagnetic fields for SERS sensors.[11] Use of diffraction-limited sources to define patterns for large oligomers or random deposition of isolated nanoparticles on surfaces has since produced ultrathin quarter-wave plates,[12] perfect absorbers,[13] and ultrafast spontaneous emission sources.[14] (Sub)nanometer gaps between plasmonic nanoparticles has led to light−matter interactions including single-molecule surface-enhanced Raman scattering (SERS) spectroscopy,[15] room-temperature single-molecule strong coupling,[16] and second-harmonic generation.[17] Yet fabrication of discrete assemblies at nanoscale (sub-100 nm) dimensions with controlled (sub)nanometer gap spacing and at high densities over large areas remains challenging.[18,19]

Long-range driving forces (~μm scale) have been used extensively in colloidal assembly, including capillary forces,[20−22] convection,[23,24] optical tweezing,[25] electrophoresis,[26] and electrokinetic phenomena (electrically driven fluid flow and particle motion).[27−30] Short-range driving forces, such as electrostatic interactions, van der Waals forces, and chemical cross-linking, are also essential to control gap spacing, which has a profound impact on the optical response of plasmonic assemblies. Of these, chemical cross-links, including DNA origami,[31−33] Cucurbit[*n*]uril,[34,35] small molecules,[36−38] protein linkers,[39,40] and polymer encapsulation[41−43] provide the most flexibility and control in architectures achieved from colloidal dispersions. Yet assemblies fabricated using chemical cross-linking methods typically do not employ long-range driving forces and rely on diffusion, often leading to low oligomer density and/or incomplete assemblies.

In this work, we use induced charge electroosmosis, also referred to as electrohydrodynamic (EHD) flow, to drive the chemical cross-linking of nanospheres on a working electrode surface under a dc potential with a counter electrode. EHD flow[44−46] is an electrokinetic phenomena that arises from lateral potential gradients within an electrode polarization layer[30] and has been studied for both ac and dc applied potentials.[47] The resultant flow can be radially attractive toward the source of the gradient; in this work a nanosphere in the lateral plane of an electrode is used to generate the gradient. EHD flow has been

primarily studied in the context of micrometer-scale particles, where particles become entrained in flow fields resulting in two-dimensional close-packed assemblies.[47] Resultant structures are transient and are typically imaged *in situ* using confocal microscopy, making it difficult to understand assembly behavior at sub-100 nm dimensions.

Interestingly, EHD flow is found here to drive chemical cross-linking of 40 nm Au nanospheres forming anhydride bonds between them. Anhydride bonds are observed spectroscopically with SERS and are consistent with gap spacings observed *via* transmission electron microscopy. Atomistic simulations elucidate that both the close proximity between nanospheres and increased residence time induced by EHD flow increase the probability that the activated isourea species will react with nearby carboxylic acids, yielding an anhydride linkage that is not commonly observed during carbodiimide cross-linking reactions.[48] By freezing transient EHD assemblies with chemical cross-linking, oligomer distributions on the surface are analyzed to provide insight into how long-range forces (EHD, Brownian motion) and short-range forces (chemical cross-linking, electrostatic inter-actions) affect assembly of nanospheres. A statistical analysis of scanning electron microscopy images shows that permanent oligomers composed of 10 nanospheres or less result when deposition favors EHD flow over random Brownian motion. The extinction response of assemblies over a large area is dominated by oligomers with gap spacings of 0.9 nm. Further probing of a large-area optical response with a standard SERS analyte demonstrates uniform enhancement factors of 10^9 with a relative standard deviation of 10% over a 1 mm^2 area. Thus, these surfaces provide the benefit of uniformity of contempo-rary lithographic[49] and roll to roll[50] fabrication of SERS surfaces while providing high signal enhancements due to 0.9 nm gap spacings in oligomers. Overall assembly is found to depend on the probability of (1) nanosphere−nanosphere collisions (influenced by EHD flow), (2) overcoming activation energy barriers (enthalpic effects), and (3) steric interactions (entropic effects), leading to appropriate molecular configurations for reactions to occur. These results demonstrate the ability to enable chemical reactions in plasmonic nanogaps with long-range colloidal driving forces. This provides interesting insights for hierarchical assembly platforms for large-area nanodevice fabrication.
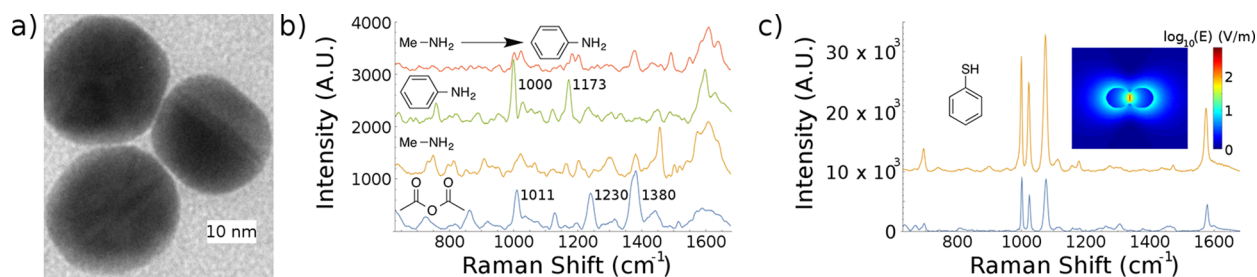
Figure 2. (a) Representative transmission electron microscopy micrograph of EHD-assembled Au nanospheres deposited on a PS-*b*-PMMA-coated graphene membrane grid. Gap spacings observed are consistent with anhydride linkers, forming from LA ligands on nanospheres. (b) SERS spectra (each offset from one another by 1×10^3 for visual clarity) of an EHD-assembled oligomer sample of an untreated sample with the anhydride groups intact (blue curve), after overnight treatment of a sample with 0.5 mM methylamine (orange curve), which cleaves anhydride groups, and aniline (green curve), which cleaves the anhydride and leaves a phenol group. No aniline signal is observed after subsequent treatment with methylamine and then aniline (red curve), and (c) when a benzenethiol (BZT) self-assembled monolayer is formed on a sample without (blue curve) and with oxygen plasma treatment (orange curve). The inset depicts the magnitude of the electric field in logarithmic scale.

RESULTS AND DISCUSSION

Electrohydrodynamic Flow Driving Chemical Cross-Linking for Oligomer Assembly. Two-dimensional growth of Au nanosphere oligomers over areas as large as 1 cm^2 occurs *via* a two-step seeded growth method where oligomer growth from Au nanosphere seeds is driven by electrohydrodynamic (EHD) flow. After growth, oligomers are stabilized by chemical cross-linking that also provides uniform gap spacings. The process of oligomer growth and cross-linking is depicted in Figure 1a, and the mechanism is as follows: (1) Electrophoretic sedimentation guides Au nanospheres toward a doped Si working electrode coated with a polystyrene (PS)-*b*-poly-(methyl methacrylate) (PMMA) diblock copolymer template. Carbodiimide cross-linking chemistry[51] covalently binds these Au nanosphere seeds on amine-functionalized PMMA regions. The PS-*b*-PMMA diblock copolymer template is composed of PMMA lamella domains with widths of 40 nm and a fractional surface coverage of 28%. The template is chosen to distribute Au monomer seeds evenly over the entire surface. (2) The presence of bound Au nanosphere monomer seeds on the working electrode promotes oligomer growth by generating EHD flow. EHD flow is a combination of electroosmotic flows that are enabled by the presence of 2.3 mM 2-(*N*-morpholino)-ethanesulfonic acid (MES) salt included in the colloidal solution. EHD flow entrains nearby nanospheres, extending approximately four particle diameters,[52] dragging them toward the source of the perturbation (the Au seed) in the plane of the electrode, leading to the growth of oligomers. A second growth step with a fresh Au nanosphere solution is used to further grow oligomers. The inset of Figure 1 illustrates the tangential, attractive EHD flow on an electrode surface near a covalently bound Au seed on PMMA. (3) As oligomers formed by EHD are transient,[47] *e.g.*, when the voltage is removed, the assembled particles will dissolve back into the bulk solution without a strong attractive force with the surface. Here, carbodiimide cross-linking chemistry stabilizes oligomers after formation. Deposition steps are limited to 10 min due to the decomposition of the activated O-acylisourea into an inert N-acylisourea, which prevents further oligomer growth.[51] While we find two deposition steps are sufficient, deposition steps may be repeated to continue oligomer growth. A substrate assembled with additional deposition steps is shown in the Supporting Information.

Chemical pathways of carbodiimide cross-linking chemistry are illustrated in Figure 1b. Au nanospheres are assembled on the surface *via* two paths. First carbodiimide activates the carboxylic acid on the particle forming the isourea species, which then forms an amide bond with PMMA, labeled Path 1. Amide bond formation with PMMA can also be accelerated with S-NHS *via* intermediate succinide formation, labeled Path 3. However, the activated isourea may also react with carboxylic acids, yielding anhydride bonds as labeled in Path 2.[51] Anhydride bond formation is not frequently observed, and, when observed, it has been attributed to the close proximity between carboxylic acid groups during polymer cross-linking[48] and related to the Thorpe–Ingold effect in cyclization reactions. Atomistic simulations show that the equilibrium distance between two gold surfaces cross-linked with anhydride linkers to be 0.85 nm. This prediction is consistent with the gap spacing between nanospheres observed in transmission electron microscopy (TEM) images (Figure 2a), which is approximately 0.9 nm. It is also important to note that the gap spacing observed is different when oligomers are assembled in the absence of applied bias; a TEM image of a dimer is shown in Figure S1 having a gap spacing of approximately 3.6 nm, which falls into the 2–7 nm range previously reported for nanospheres assembled without an applied bias.[11] The observed gap spacing in Figure S1 is just greater than twice the length of the lipoic acid (LA) ligands. All substrates are assembled in a 2.3 mM electrolyte solution, resulting in an electrostatic potential barrier between nanospheres.

While the TEM results support anhydride bond formation, it is also possible to spectroscopically probe molecules between nanospheres. Surface-enhanced Raman scattering (SERS) spectra provides a means to interrogate molecules near the center of the gap, where the electric field intensity is maximum. Figure 2b (lower blue curve) depicts a SERS spectrum of a sample with 40 nm Au oligomers on the surface prepared as described in the Methods Section. Vibrational bands associated with anhydride groups are observed at 1011, 1230, and 1380 cm^{-1}, corresponding to the C–H rocking, C–O stretch, and C–H scissoring modes, respectively.[53,54] These vibrational bands are used to identify anhydride moieties, as there is good contrast with carboxylic acid moieties[55−57] and little overlap with N-acylisourea vibrational modes.[58] We probe the ability to monitor local chemistry in the gap by cleaving anhydride linkages *via* nucleophilic substitution. The orange curve in Figure 2b depicts a SERS spectrum observed after overnight
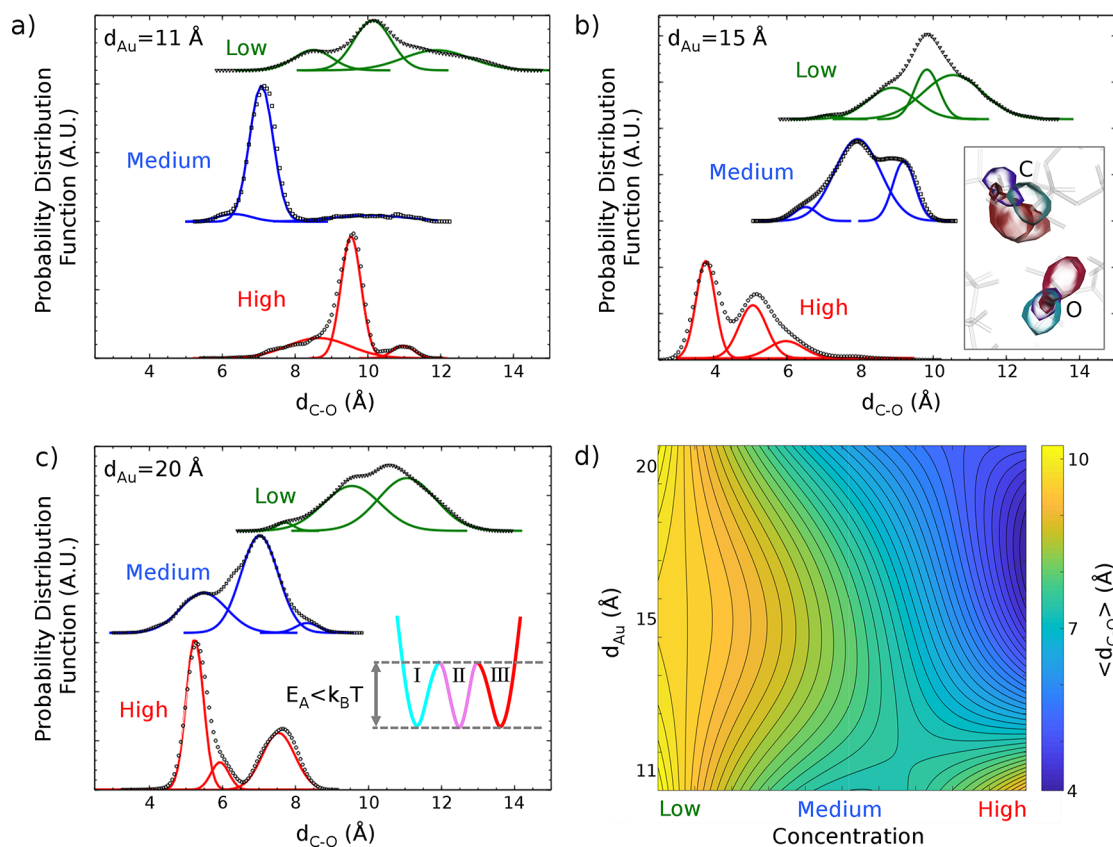
Figure 3. Analysis of the distribution of C−O distance, d_{C-O}, corresponding to the reactive carbon atom in OA and the deprotonated oxygen atom in LA for low (one OA + one LA), medium (one OA + four LA), and high (two OA + four LA) concentrations. OAs and LAs are interacting in the aqueous medium between two Au surfaces that are separated at d_{Au} (a) 11, (b) 15, and (c) 20 Å. Gaussian mixture analysis indicates the presence of three distinct degenerate d_{C-O}. The inset in (b) represents superposition of the degenerate states that are depicted by red, violet, and cyan regions corresponding to three distributions of d_{C-O} averaged at 3.8, 5, and 6 Å, respectively. Water molecules are not displayed, and OA and LA are shown in gray color for the sake of clarity. The inset in (c) provides a schematic representation of the energy landscape consisting of three states separated by energy barriers comparable to thermal fluctuations. (d) Color-map of the average d_{C-O} as a function of concentration and d_{Au}. The minimum average distance has an entropic nature as a result of competition between concentration and steric interactions.

treatment of a sample with 0.5 mM methylamine, a molecule with weak Raman bands.[59] Notably the vibrations associated with anhydride groups no longer stand out above the background, indicating they have been cleaved by methylamine. In order to further probe chemistry in the gaps, nucleophilic substitution of the anhydride linker with aniline, a molecule with a higher Raman cross section than methylamine, is examined. The green curve in Figure 2b depicts a SERS spectrum observed after overnight treatment of a sample with 0.5 mM aniline. Characteristic peaks are observed at 1000 and 1173 cm^{-1}. For comparison, subsequent treatment of first methylamine (to cleave anhydride bonds) and then aniline (where selective attachment in the hotspot will now not occur since anhydride bonds have been cleaved) indeed shows a much weaker SERS signal for aniline. This spectrum is shown in the top red curve of Figure 2b. Here any indication of aniline in the spectrum would be due to binding to the gold surface via amine−Au interactions. This does not appear to be occurring at a significant rate, and this is reflected in the SERS spectrum. The SERS spectra showing the presence of vibrations associated with anhydride groups and then aniline groups indicate molecules can be placed in the gaps via a reaction with the cross-linking molecular group. Thus, the cross-linking

chemistry used to assemble oligomers also enables sensing of nucleophilic compounds.

The SERS data of Figure 2b demonstrate that functional groups used for chemical assembly and other molecules in the gaps are observable in spectra due to high electric field enhancement in the nanometer gaps. Full-wave finite elements method simulations show an electric field enhancement on the order of 600 in the hotspot region of a dimer due to the narrow gap spacing; the electric field profile on a cross section passing through the middle of the dimer is shown on a logarithmic scale in the inset of Figure 2c. We can also measure field enhancements using a standard Raman reporter molecule, benzenethiol (BZT). Figure 2c (lower curve) shows SERS spectra of an oligomer sample after exposure to BZT. Yet if anhydride bonds reside in the "hottest" region, BZT cannot access this region. An oxygen plasma treatment is then performed to remove ligands from nanosphere surfaces, and a SERS spectrum is again acquired after BZT exposure onto the nanospheres' surface; the spectrum is shown in the upper curve of Figure 2c. After oxygen plasma treatment, the SERS signal from BZT increases up to 258%. The increased SERS signal is concomitant with the increased hotspot occupation volume by BZT and can be attributed to diffusion of BZT into the hotspot that is possible after removal of the anhydride from the gaps
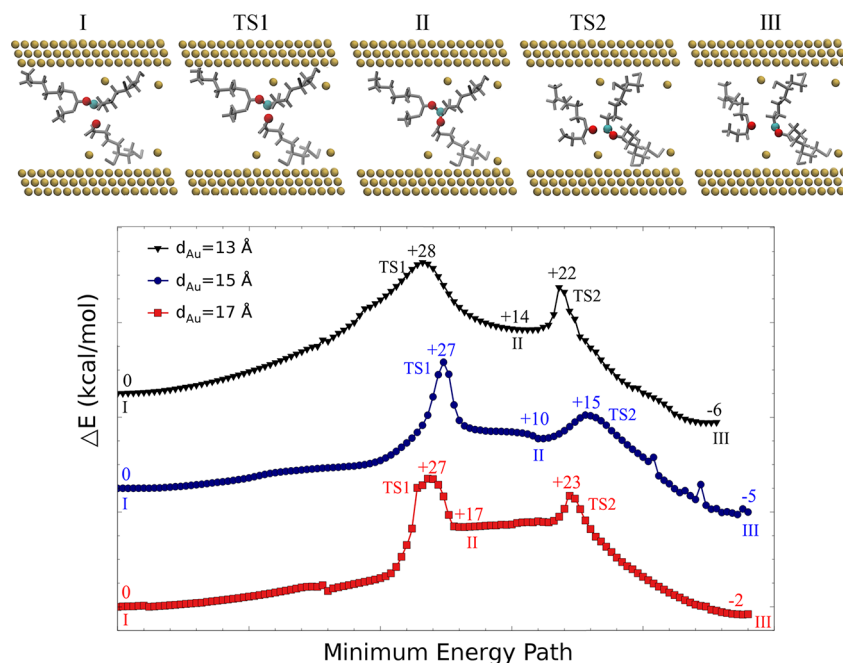
Figure 4. Minimum energy path of OA and deprotonated LA reaction obtained from nudged elastic band (NEB) calculations at d_{Au} = 13, 15, and 17 Å. The initial (I), intermediate complex (II), and final states (III) are separated *via* two reaction energy barriers, transition states TS1 and TS2. The top schematics provide a snapshot of these states extracted from NEB calculations. The reactive carbon and oxygen atoms are highlighted respectively in blue and red, while the rest of the organic molecules are shown in silver, and water molecules are omitted for clarity. The activation energy, E_a, is estimated to be around 27 kcal/mol for TS1 and 5−8 kcal/mol for TS2.

between nanospheres. Interestingly, comparison of the 1076 cm^{-1} in-plane ring deformation superimposed with the C−S stretch and the 998 cm^{-1} in-plane ring deformation shows greater enhancement of the 1076 cm^{-1} band after removing the anhydride linker; the two peaks show approximately equal intensity in SERS data before plasma etching. This further indicates that the C−S bond has displaced the anhydride previously located in the hotspot, as the relative intensity of the vibrational modes is related to the molecular orientation in the gap. The ability to remove anhydride groups in the gaps is important for label-free SERS sensing applications, where analyte molecules in hotspots will yield lower detection limits.

Reactive molecular dynamics (MD) simulations illuminate the origin of the EHD-driven anhydride cross-linking. The stability of Au nanospheres in solution with a carbodiimide cross-linker indicates that the anhydride pathway is a rare event.[60] We examine this hypothesis by analyzing the probability distribution function of the distance between the reactive carbon atom in acylisourea (OA) and the deprotonated oxygen atom in lipoic acid (LA) (d_{C-O}) using the transferable ReaxFF potential.[61,62] The exact concentration of LA and OA ligands on the surface may vary from nanosphere to nanosphere, so three concentrations are analyzed: one OA to one LA (low), one OA to four LA (medium), and two OA to four LA (high) concentrations. The concentrations investigated are in the range of LA ligands observed on the surface of gold nanospheres.[63] In simulations, ligands are connected to opposing faces of a Au (111) slab at 11, 15, and 20 Å nanogap separations, d_{Au}. Simulation parameters are further detailed in the Methods Section. Figure 3a−c (dotted curves) depict the distributions of d_{C-O} in the various cases, with Figure 3d providing an interpolated contour map of the relationship between d_{Au}, d_{C-O}, and ligand concentration. Two features of the nanogap chemistry are salient: (1) 17 Å corresponds to

fully extended LA and OA ligands and is thus the minimum d_{Au} for the reaction to occur. This minimum distance for reaction is not observed in TEM images obtained from control samples assembled without EHD flow. (2) Regardless of ligand concentration and d_{Au}, the proximity required for reaction (d_{C-O} = 2.9 Å) is at least 4 standard deviations from the mean d_{C-O}. These results indicate that EHD flow is necessary for maintaining close proximity between nanoparticles in time-frames reasonable for reaction.

Interesting ligand dynamics also emerge from the MD study, indicating entropy's role in this reaction. Gaussian mixture analysis of d_{C-O} trajectory, depicted in Figure 3a−c as solid curves, identifies three normal distributions regardless of concentration and nanogap distance. The inset of Figure 3b visualizes these states in red, violet, and cyan in the configuration space. These three states are separated by energy barriers comparable to thermal fluctuations, k_BT, schematically illustrated in Figure 3c's inset. MD simulations probe these three degenerate states *via* a diffusive mechanism, which is entropic in nature. We find that the average d_{C-O} decreases with increasing concentration except for the case of high concentration at small nanogap distances, d_{Au} = 11 Å. The latter is strongly affected by the presence of large steric forces between OA and LA groups that ultimately hinder the mobility of reaction sites in the nanogap. The minimum average proximity, d_{C-O} = 4.1 ± 0.3 Å, occurs at high concentration, when the nanogap separation is 15 Å. Yet, this distance is greater than the proximity required for reaction, 2.9 Å, and only the tail end of the probability distribution function samples this space. Therefore, we can conclude that entropic effects play a critical role in bringing reactive cores in proximity to each other, an event that occurs rarely as a result of competition with steric effects. Furthermore, our results confirm that the probability of bringing reactive groups in proximity to one
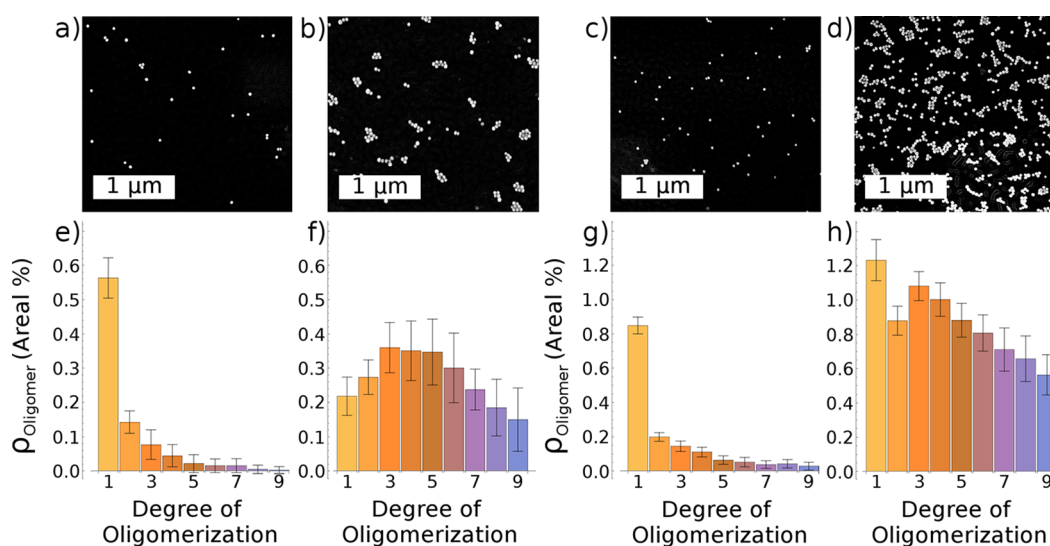
Figure 5. Representative SEM images taken from the substrate surfaces with 40 nm Au nanospheres deposited at (a, b) room temperature and (e, f) corresponding oligomerization distribution observed on control substrates and EHD-anhydride substrates, respectively. The close packing of oligomers and reduction of monomer observed on EHD-anhydride substrates are the hallmark of EHD flow driven oligomerization. (c, d) Representative SEM images and (g, h) corresponding oligomerization distribution observed on 60 °C control substrates and 60 °C EHD-anhydride substrates, respectively. Nanosphere surface density is seen to increase greatly with increased Brownian motion of the particles. The 60 °C EHD-anhydride substrate is observed to have a reduced degree of oligomerization compared to the room-temperature EHD-anhydride substrate.

another is dependent on both the concentration and nanogap size, $P_{entropy} = P_{entropy}(C, d_{Au})$, hypothesized in previous work to drive anhydride bond formation *via* carbodiimide cross-linking.[48]

With the role of entropy understood, we turn now to consider enthalpic processes. Observation of rare chemical reactions with the MD framework is facilitated *via* a harmonic bias potential that favors small d_{C-O}. At high temperatures anhydride formation is indeed observed, consistent with the premise that EHD flow is necessary to facilitate this reaction. A nudged elastic band (NEB) technique is employed[64,65] to probe the minimum energy path (MEP), given low d_{C-O}. Figure 4 depicts the MEP of low concentration LA-OA (I) reaction to form an anhydride (III), exhibiting two enthalpic reaction barriers (TS1 and TS2) and a metastable intermediate complex (II) at different d_{Au}. The configurations at the top of Figure 4 provide a schematic representation of successive reaction stages extracted from NEB simulations. The enthalpy of reaction is found to vary between −2 and −6 kcal/mol, indicating an exothermic process. The TS1 activation energy barrier is roughly 27 kcal/mol (~45 $k_B T$ at ambient conditions) irrespective of d_{Au}. This activation energy is comparable to that of imine carbons on polycarbodiimides measured in ^{13}C CP/ MAS NMR spectroscopy.[66] The intermediate complex further dissociates to yield anhydride with a TS2 activation energy barrier estimated at 5−8 kcal/mol. NEB calculations indicate that transition through TS1 is the rate-controlling step in the anhydride formation. This enthalpic rate is controlled neither by the concentration nor by the nanogap size. Therefore, the probability of such enthalpic reaction, in terms of external variables, is just a function of temperature, $P_{enthalpy} = P_{enthalpy}(T)$, in our system. Thus, the probability of reaction $P_{Reaction} = P_{entropy}(C, d_{Au}) \times P_{enthalpy}(T) \times P_{Collision}$ is tuned on the nanosphere assembly surface by modifying $P_{Collision}$ *via* EHD flow.

Investigation of Driving Forces in Assembly. In the prior section, investigations were performed to understand how EHD flow enables cross-linking chemistry of nanospheres and controls gap spacings in oligomers. Here we investigate how EHD flow induced anhydride cross-linking affects density and geometry of oligomers on substrates; hereafter we refer to samples as EHD-anhydride substrates. This analysis is aided by examining oligomer formation on substrates assembled without applied bias, hereafter referred to as control substrates. Figure 5a,b depict representative SEM images of substrate surfaces assembled at room temperature without and with an applied bias, respectively. First it is important to consider how oligomers form on control surfaces. In the case of zero bias-voltage deposition, amine-functionalized copolymer-coated Si substrates are placed in a carboxylic acid-functionalized Au nanosphere colloid with carbodiimide cross-linker. Brownian motion drives the nanospheres to randomly collide with the substrate surface. Similar to Au seed assembly, collisions can result in a reaction between an *O*-acylisourea on the nanosphere and an amine on the surface, covalently binding nanospheres to the PMMA domains *via* an amide bond. An oligomer is formed when another nanosphere reacts with the PMMA surface near a monomer. The tendency to grow beyond a monomer is referred to as oligomerization. Oligomer configuration (measured as number of nearest neighbors) and oligomerization are examined by measuring percent coverage of various oligomers (monomer, dimer, trimer, *etc.*) on the substrates' surfaces. Percent coverage statistics are determined *via* analysis of SEM images over 25 adjacent regions with dimensions 8.0 μm × 5.5 μm as detailed in the Supporting Information, Figure S2. Coverage statistic data are shown in Figure 5e,f. We find, unsurprisingly, that control substrates exhibit a steep decrease in percent coverage beyond a monomer, due to electrostatic repulsion between nanospheres, and a monotonic decrease in percent coverage beyond a dimer.

Comparison of statistics in Figure 5e and f shows a 336% increase in nanosphere coverage is observed on the EHD-anhydride substrate with respect to the control. The increase in coverage can partially be attributed to electrophoretic sedimentation due to the applied bias. Yet examination of Figure 5e and f also shows dramatically increased oligomerization, few monomers, and many close-packed oligomers, a signature of EHD flow driven assembly, on the EHD-anhydride substrate. The average number of nearest neighbors per particle increases from 0.66 to 2.2 (where 0 is an isolated particle and 6 is a 2D hexagonally close-packed lattice) from the control to the EHD-anhydride substrate. If electrophoresis was the only driving force, surfaces would exhibit a monotonically decreasing oligomerization distribution similar to the control substrate. Instead, the distribution is centered around quadrumers in Figure 5f, and anhydride linking induced by EHD flow leads to over a 2.5-fold reduction in the number of monomers with respect to the control substrate. This observation is consistent with the seeded growth assembly mechanism where seed monomers are consumed when they oligomerize *via* anhydride attachment with nanospheres in a colloid due to the presence of an applied bias driving EHD flow.

It is also important to consider how Brownian motion competes with EHD flow during oligomer formation. The effect of Brownian motion can be evaluated by examining oligomer configuration statistics after assembly when the colloid is heated to 60 °C during deposition; representative images are shown in Figure 5c,d for both control and EHD-anhydride substrates, respectively. Without voltage, Figure 5c, one observes a nearly 2-fold increase in the number of nanospheres attached to the surface in comparison to room-temperature deposition (Figure 5a). With voltage, Figure 5d, one observes a dramatically increased density of oligomers, with respect to all other assembly conditions. The total nanosphere surface coverage for the 60 °C EHD-anhydride substrate is 15%, while the surface coverage for the room temperature EHD-anhydride substrate is 3.7% (shown in Figure 5b). Figure 5g,h depict the oligomerization statistics obtained from the control and EHD-anhydride substrates, respectively, to understand the more complex behavior at elevated temperature. First Brownian motion is expected to increase the number of nanosphere collisions with the surface, increasing the number of monomer seeds. Monomers indeed dominate in frequency on the 60 °C control substrate, as observed in the SEM image in Figure 5c and statistics in Figure 5g. The EHD-anhydride substrate deposited at 60 °C shows a reduced degree of oligomerization (see Figure 5h) when compared to the room-temperature EHD deposition (shown in Figure 5f). There is a slight shift to smaller oligomers on average; trimers are observed with the higher frequency over quadrumers when deposition occurs at 60 °C *versus* room temperature. Oligomers are still observed to be close packed, with an average of 2.06 nearest neighbors per particle, indicating EHD is still a major long-range driving force in assembly at 60 °C. These data unsurprisingly indicate that EHD flow competes with Brownian motion, yet Brownian motion does not completely overwhelm EHD flow in determining oligomer morphology during assembly of nanospheres of 40 nm diameter. Indeed, the increase in temperature is a means for limiting the size of oligomers and increasing their density on the surface by increasing the number of seed monomers on the template surface. For many applications, for example SERS sensors, the higher surface coverage of the EHD-anhydride substrate

prepared at elevated temperature is desirable for high hotspot density. The increased oligomer density and reduced degree of oligomerization from a slight increase in deposition temperature synergistically improve optical response uniformity, as we shall see in the following section.

The relative contributions of EHD flow, Brownian motion, and electrophoretic sedimentation can be further elucidated by comparing oligomerization of particles with different dimensions.[67] While long-range forces associated with EHD flow (Brownian motion) increases (decreases) with increasing particle diameter, electrophoretic mobility is primarily dependent on zeta potential.[68] Figure 6a,b are representative SEM
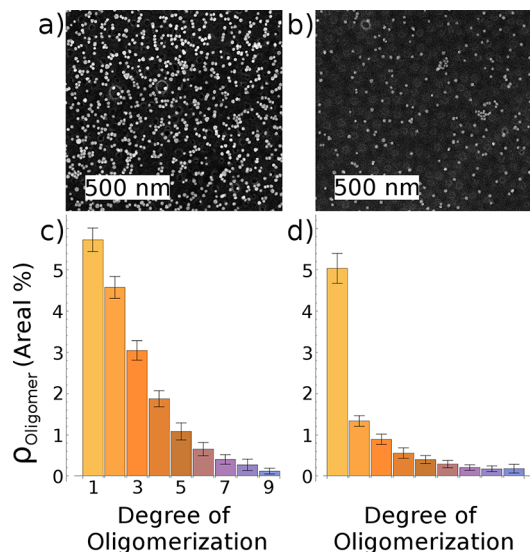
Figure 6. Nanosphere oligomer substrates assembled with 20 nm diameter Au nanospheres. (a, b) Representative SEM images taken from the substrate surfaces and (c, d) the oligomerization distribution observed on room-temperature and 60 °C EHD-anhydride substrates, respectively.

images and oligomerization statistics from room-temperature and 60 °C depositions, respectively, performed with 20 nm diameter Au nanospheres. All other deposition parameters are identical to the 40 nm diameter Au nanosphere EHD-anhydride depositions. Figure S3 depicts a TEM micrograph of 20 nm diameter particles on a room-temperature EHD-anhydride assembled substrate showing the characteristic ~1 nm gap. Oligomerization statistics depicted in Figure 6 c,d are determined from 25 SEM images with dimensions of 4.0 μm × 2.7 μm. The room-temperature sample has significantly greater total surface coverage than its 40 nm diameter counterpart, 17% compared to 3.7%, likely due to the reduced Stokes drag on the smaller particles.[68] Figure 6d shows that increasing heat to 60 °C greatly reduces EHD flow induced oligomerization; this is likely due to the significant increase of the average velocity of the 20 nm particles at the higher temperature. These data show that increased Brownian motion competes with EHD flow, and the faster moving nanospheres have a reduced probability of being entrained by EHD flow. Overall the 20 nm diameter substrates are significantly less oligomerized than the 40 nm substrates, which is consistent with the fact that EHD flow force density scales with particle size; 20 nm diameter appears to be the lower limit in which EHD flows are an important driving force for colloidal assembly, consistent with observations using optoelectrokinetic flows.[69]
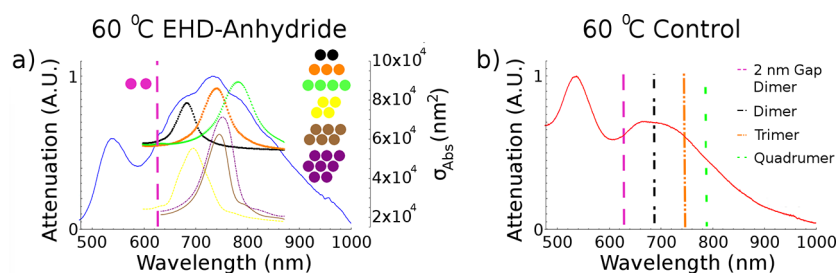
Figure 7. Normalized attenuation spectra of a 40 nm (a) 60 °C EHD-anhydride substrate (solid blue curve) and (b) 60 °C control (solid red curve). The spectrum in (a) is overlaid with the calculated absorption cross section of observed oligomers with various geometries with a color-coded schematic. Close-packed absorption cross sections are offset by 3.9×10^4 for visual clarity. Clearly resolved dimer, trimer, and quadrumer peaks within the attenuation spectrum are indicative of the anhydride cross-linking, which maintains gap spacings within oligomers. In (b) the calculated maximum values of the absorption cross section of a linear dimer, trimer, and quadrumer with 0.9 nm gap spacings are shown with black, red, and green lines, respectively.

Optical Response of EHD-Anhydride Substrates. The motivation for utilizing a long-range driving force to induce chemical cross-linking is uniformity of coverage over large areas. UV−vis spectroscopy is used to probe the large-area optical response of EHD-anhydride substrates with 40 nm Au nanospheres. An area of 9 mm × 0.5 mm was measured, and normalized attenuation spectra of 60 °C EHD-anhydride and, for comparison, control substrates are plotted in Figure 7a,b, respectively. Samples are prepared on transparent conductive substrates as detailed in the Methods Section and immersed in water during measurements. The absorption spectra of differing oligomer geometries with 0.9 nm gap spacings are simulated with the full-wave finite element method and overlaid as dotted and dashed curves with the measured attenuation spectrum in Figure 7a. This allows us to examine how different geometries contribute to the measured attenuation spectrum.

Four distinct peaks are readily observable within the 60 °C EHD-anhydride substrate's attenuation spectrum. Simulations identify these peaks to be associated with monomers (536 nm, in good agreement with Mie scattering theory), dimers (686 nm), trimers (740 nm), and quadrumers (782 nm) with 0.9 nm gap spacings. These results indicate that the large-area optical response is dominated by anhydride-linked oligomers with characteristic 0.9 nm gap spacing. This is further corroborated by examining the attenuation spectrum of the 60 °C control substrate, shown in Figure 7b. Unsurprisingly the spectrum is dominated by monomer attenuation. Lines representing the absorption maximum, determined from full-wave simulations of dimers, trimers, and quadrumers, are also depicted in Figure 7a,b for visual clarity. No discrete oligomer peaks can be observed in the UV−vis spectrum from the control sample. Consider that the absorption maximum of a 2 nm gap dimer geometry, calculated in simulations and plotted with a dashed line in Figure 7a, the dimer absorption peak is shifted by nearly 50 nm from the 0.9 nm dimer case. The blurring of the oligomer response for the control substrate is attributed to the lack of anhydride-mediated control of gap spacings, which results in a continuous distribution of spectral position for any given oligomer geometry.

Interestingly, UV−vis data and simulations demonstrate that oligomer gap spacings have a more profound impact on the spectral shift of an oligomer resonance than oligomerization. These results are unsurprising when one considers that the plasmon mode is only slightly perturbed by the addition of a nanosphere on an oligomer when it is not in the polarization direction of the incident excitation beam.[70] Consider the spectral position in the simulated absorption spectra of Figure

7a of a linear trimer that is shown in the curve composed of orange squares is only blue-shifted by 4 nm from a hexamer, shown in the brown curve. Adding two more particles to this configuration, shown in purple, results in a further 3 nm spectral shift. This is a much smaller broadening than occurs when the gap spacing increases from 0.9 nm to 2 nm. This observation is key to understanding why the optical response is narrower than one might expect from the oligomerization statistics in Figure 5d. As EHD flow drives the formation of close-packed oligomers, most oligomers have between three and four particles along any given polarization axis. Consider that the first circular perfectly close packed oligomer to have greater than four particles in a row contains 21 particles; 98% of oligomers observed in the 60 °C EHD-anhydride substrate contain fewer than 21 particles. More significantly, the distribution statistics by number show that 93% of the surface is composed of oligomers of nine nanospheres or less. Thus, the clear majority of oligomers can be excited with a laser wavelength between the linear trimer and linear quadrumer resonance wavelengths. The peak maximum observed in the UV−vis absorption data of Figure 7a is associated with a trimer. By exciting a surface with densely packed oligomers, observed for example in Figure 5d,h, we can expect to excite a reproducible distribution of oligomers in any given laser spot diameter.

In order to further examine the optical uniformity, a SERS enhancement factor (EF) map was acquired over 1 mm² of an oxygen plasma treated 60 °C EHD-anhydride substrate when excited with a 785 nm laser source at 76 µW for 0.1 s exposure times, shown in Figure 8. The small gap spacings in oligomers enabled by the (cleavable) anhydride cross-linker provided by template-seeded EHD flow should yield a model system for SERS. The EF is determined by assembling a self-assembled monolayer of BZT onto the substrate and observing the intensity of the 1573 cm⁻¹ vibration band. The raw SERS data are converted into an EF using the following equation:[11,71]

$$\text{EF} = (I_{\text{SERS}}/N_{\text{SERS}})/(I_{\text{neat}}/N_{\text{neat}}) \quad (1)$$

where I_{SERS} is the SERS intensity from the sample, I_{neat} is the neat Raman intensity from the bulk solution, N_{SERS} is the number of molecules participating in the SERS, and N_{neat} is the number of molecules participating in neat measurements. The number of BZT molecules participating in the SERS measurements is determined through the average surface coverage of nanospheres assumed to be coated with a self-assembled monolayer of BZT[72] over the mapped region, obtained using
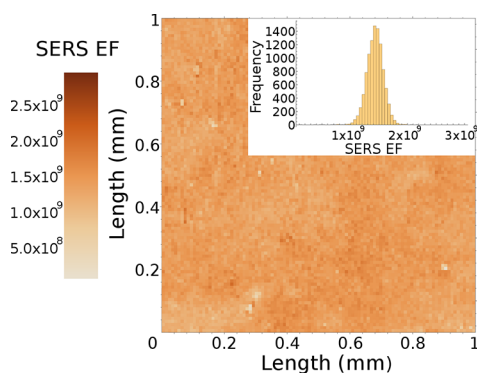
Figure 8. SERS EF map of an oxygen plasma treated 60 °C EHD-anhydride substrate across a 1 mm × 1 mm area where each measurement is separated by 10 μm, corresponding to 10 000 measurements. The laser power is 76 μW with a 0.1 s exposure time. Inset: Histogram of measured SERS EF values with 57 bins depicting a mean of 1.4×10^9, full width at half-maximum of 3.5×10^8, and RSD of 10%.

SEM images. The average coverage is used for all EF calculations. The SERS map shows an average SERS EF value of 1.4×10^9. The data show a 10% relative standard deviation (RSD) of the 1573 cm^{-1} peak across the mapped area. The SERS EF is approximately proportional to the electric field enhancement taken to the fourth power, indicating that the anhydride-linked oligomers achieve extraordinarily large electric field enhancements while providing point-to-point uniformity in the spot size of the optical beam. The low signal deviation is a result of the seeded growth oligomerization protocol that is optimized by controlling the temperature, block copolymer template, and EHD flow.

CONCLUSION

In this work, we propose a method for the seeded chemical assembly of discrete oligomers with high density over large areas. Electrohydrodynamic (EHD) flow is found to serve as a long-range driving force to bring Au nanospheres together, enabling local chemical cross-linking at an electrode surface using carbodiimide chemistry. We confirm the anhydride linker assembly mechanism with surface enhanced Raman scattering (SERS) spectroscopy and show with transmission electron microscopy that the resulting gap spacings between particles are 0.9 nm only when an applied bias is present to generate EHD flow. Parameters affecting assembly are elucidated by atomistic simulations. The probability of forming an anhydride bond between nanospheres is the product $P_{Reaction} = P_{entropy}(C, d_{Au}) \times P_{enthalpy}(T) \times P_{Collision}$, where EHD flow is a key factor to increase the probability of nanosphere–nanosphere collisions. The effect on oligomer bulk optical response is observed with UV–vis microscopy. Individual oligomer contributions to optical response is elucidated with electromagnetic full-wave simulations where it is found to depend more strongly on nanogap dimensions *versus* oligomer geometry. Finally, the electric field enhancement produced by oligomers, as determined with SERS, is shown to be relatively uniform over a 1 mm^2 area, with a relative standard deviation in signal of 10%. This is significant, as the SERS enhancement factor has an average value of 1.4×10^9. There are typically trade-offs between uniformity and high electric field enhancements in SERS measurements. The results demonstrate that the use of long-range driving forces to drive chemical cross-linking

between nanospheres represents a tool for scientists and engineers to fabricate plasmonic devices using colloidal assembly. In future work, this tool can be extended to templated assembly, permitting precisely defined EHD flow fields for fabricating uniform oligomer structures and metasurfaces.

METHODS SECTION

Materials. Random copolymer poly(styrene-*co*-methyl methacrylate)-α-hydroxyl-ω-tempo moiety (PS-r-PMMA) (M_n = 7400, 59.6% PS) and diblock copolymer poly(styrene-*b*-methyl methacrylate) (PS-*b*-PMMA) (M_n = 170-*b*-144 kg mol^{-1}) were purchased from Polymer Source, Inc. (Dorval, Canada). Gold nanospheres of diameter of 20 and 40 nm with lipoic acid functionalization were purchased from Nanocomposix (San Diego, CA, USA). Si(001) wafers with a resistivity of 0.004 ohm-cm were purchased from Virginia Semiconductor (Frederickburg, VA, USA). Hydrofluoric acid (HF) was purchased from Fisher Scientific (Pittsburgh, PA, USA). 2-(*N*-morpholino)ethanesulfonic acid (MES) 0.1 M buffer, 1-ethyl-3-[3-(dimethylamino)propyl]carbodiimide hydrochloride (EDC), and *N*-hydroxy sulfosuccinimide (s-NHS) were purchased from Pierce (Rockford, IL, USA). Dimethyl sulfoxide (DMSO), ethylenediamine, benzenethiol, toluene, ethanol, isopropyl alcohol (IPA), aniline, methylamine, potassium carbonate, and 52-mesh Pt gauze foil were all purchased from Sigma-Aldrich (St. Louis, MO, USA). Nanopure deionized water (DI) (18.2 MΩ cm^{-1}) was obtained from a Milli-Q Millipore System. Single-layer graphene on ultrafine mesh copper TEM grids and 50 mesh copper TEM grids were purchased from Ted Pella.

Nanoantenna Oligomer Substrate Fabrication. Lamella PS-*b*-PMMA block copolymer is spin-coated onto a HF-cleaned, heavily doped Si wafer and annealed as described in previous work.[11] PMMA regions are selectively functionalized with amine end groups by first immersing the entire substrate in DMSO and then in ethylenediamine/DMSO solution (5% v/v), both for 5 min without rinsing between steps. The Si substrate coated with functionalized copolymer is then washed with IPA for 1 min and dried under nitrogen.

A Au nanosphere solution (0.1 mg/mL, 3 mL) is added to a 10 mL glass beaker. Freshly prepared s-NHS (20 mM) in a MES (0.1 M) buffer (35 μL) is added to the beaker and swirled. Next, freshly prepared EDC (8 mM) in a MES (0.1 M) buffer (35 μL) is added to the beaker and swirled. For heated samples, the beaker is placed on a hot plate and brought to 60 °C. Similar to previous work[73] a 1 cm × 1 cm functionalized copolymer-coated Si substrate is placed into the solution vertically and held in place as the anode with alligator clips that do not contact the nanosphere solution. One millimeter away from the substrate, a 1 cm × 1 cm Pt mesh is placed into the solution vertically and held in place as an anode with alligator clips that do not contact the nanosphere solution. A dc regulated power supply is used to apply a voltage of 1.2 V for 10 min. The substrate, Pt mesh, and beaker are rinsed with IPA for 1 min and dried under nitrogen. This process is repeated with the same substrate and fresh nanosphere solution as described above, but with 25 μL of EDC and s-NHS solution. Two growth steps are necessary to obtain oligomers on resonance at the 785 nm illumination wavelength used for SERS measurements. The second growth step is performed with reduced EDC and s-NHS concentrations to promote anhydride formation, which has been shown to increase with decreased concentration.[74] Oxygen plasma treated samples are treated with a 50 W oxygen plasma etch for 120 s.

Assembly on Alternative Substrates. Substrates fabricated for TEM characterization are fabricated as above, but on copper TEM grids for field-free control substrates and graphene membrane TEM grids for EHD-anhydride samples. PS-*b*-PMMA block copolymer templates on indium tin oxide (ITO)-coated glass are fabricated identically, but using ITO-coated glass that is oxygen plasma etched at 100 W for 1 min instead of the Si wafer.

Characterization. After nanoantenna oligomers are assembled onto their respective substrates, images are collected with a Magellan XHR SEM (FEI) and a CM-20 TEM (Philips).

UV−vis absorption spectra are taken of nanoantenna oligomers on ITO-coated glass substrates taped (away from the beam path) onto a quartz cuvette. The cuvette is then filled with water and imaged with a Shimadzu UV-1700 absorption spectrometer.

Raman spectroscopy measurements are conducted using a confocal Renishaw InVia micro Raman system with a laser excitation wavelength of 785 nm. All SERS measurements are taken at 73 μW with exposure of 0.1 s for map measurements and 1 s for individual spectra on 60 °C EHD-anhydride substrates. All measurements use a 60× water immersion objective with a 1.2 NA, immersed in DI water. SERS enhancement factors are calculated according to the method of Cai *et al.*[75] Briefly, N_{SERS} is estimated by determining the average surface area of Au *via* SEM and using an experimentally determined density of BZT on Au surfaces Aggarwal *et al.*[72] N_{Neat} is determined by aliquoting neat BZT onto a Si wafer and a glass coverslip affixed on top. The effective height of the BZT (4.07 μm) is determined by measuring the Raman intensity−depth profile, and the bulk density of BZT is used in the calculation. As both the neat and SERS measurements are obtained with the same microscope objective, the EF is not a function of spot size. I_{SERS} and I_{NEAT} are normalized by laser power and acquisition time. Neat BZT measurements are taken with the same laser and a 60× water immersion objective but with 73 mW laser power and 10 s exposure time.

Finite Element Simulations. Full-wave simulations (frequency domain finite elements method solver) are implemented in CST Microwave Studio (CST AG). Absorption spectra are simulated for several nanosphere oligomers: dimer, linear trimer, linear quadrumer, close-packed quadrumer, close-packed hexamer, and close-packed octamer. Au nanospheres with a diameter of 40 nm are used with permittivity from the Drude model with parameters extracted from Grady *et al.*[76] We use a 0.9 nm gap between nanospheres, consistent with both observed and the modeled length of an anhydride linker. The nanospheres were previously shown to be partially embedded in PMMA,[73] with the PMMA layer thickness set to 40 nm and the center of the nanospheres 8 nm above the layer. Below the PMMA layer is a 150 nm layer of ITO on top of a 2 μm layer of glass. The relative electric permittivity of water, PMMA, glass, and ITO used in the simulations are 1.77, 2.47, and 2.3207, and adapted from Moerland *et al.*,[77] respectively. The permittivity in the gap region is uncertain, as the excitation source will probe a volume composed of the anhydride linker, aqueous solution, and copolymer environment. In order to account for this, a parameter sweep of the gap permittivity is performed using the dimer configuration, and the permittivity that best corresponds to the observed dimer structure peak at 686 nm is determined to be 2.25. This parameter is reasonable based on an estimate of the average permittivity of the materials[78] and further verified by the correspondence between the trimer configuration's simulated plasmon resonance and the trimer peak observed in the EHD-anhydride sample.

Oligomers are excited with plane wave illumination at normal incidence with electric field polarization along the axis of the linear oligomers, and the absorption cross section of the structure is determined.

Atomistic Simulation. We construct a periodic supercell containing a total of 288 gold atoms arranged in six layers of a (111) plane. The simulation box dimensions in the *xy* plane are roughly 20 Å × 17 Å. The size of the simulation cell in *z* dimension varies between 23 and 32 Å to provide different nanogap distances. We change the number of water molecules from 30 to 120 to fill the free space between organic molecules in the nanogap. The number of water molecules depends on the concentration of organic molecules and gold surface-to-surface distance. We first construct all organic molecules, both lipoic acid and *O*-acylisourea, in AVOGADRO software[79,80] and minimize the configurations using the UFF force field.[81] We subsequently insert these organic molecules inside the nanogap such that sulfur atoms are next to the gold surface. We perform our simulations using the ReaxFF potential,[62] a reactive force

field designed based on the notion of bond-order parameter[82,83] and the electronegativity equalization method[84] to update variable charges at each step of the atomistic simulation. Here, we use a transferable set of ReaxFF parameters that were trained for biomolecules and their interaction with gold surfaces.[61] We use the LAMMPS simulation package in all MD calculations.[85] MD simulations are carried out in the canonical (NVT) ensemble using a Nosé−Hoover thermostat[60] with a relaxation constant of 0.01 ps. The time step in MD simulations is set to 0.1 fs.

In simulations for carbon−oxygen distance analysis, we construct nine periodic simulation boxes with gold−gold surface distances of 11, 15, and 20 Å, each containing three levels of OA−LA concentrations. In low and medium concentrations respectively, we attach one OA to one side of the Au slab, while we place one and four LA molecules at the other surface. For the high-concentration case, two OA molecules on one side face four LA groups on the other side of the gold slab. We adjust the number of water molecules in each simulation to achieve ambient conditions at equilibrium. We first perform potential energy minimization to relax the structure. We subsequently relax the position of the water molecules in a 20-ps-long MD simulation, while the rest of the atoms are fixed in their position. Afterward, we further relax the system in canonical ensemble for 100 ps. A 400-ps-long production phase produces the MD trajectory saved at intervals of 0.1 ps.

For MEP simulations, we first construct three simulation boxes with nanogaps of 13, 15, and 17 Å. We place one OA molecule on one surface and one LA group on the other. We adjust the number of water molecules to obtain ambient pressure at equilibrium. The purpose of these simulations is to capture a reasonable initial and final state on each side of the energy barrier for NEB calculations. To accelerate the formation of the intermediate state, we apply a bias harmonic potential between reactive carbon and oxygen atoms. This spring should be strong enough to keep the reactive core in the proximity of the transition state. Also, a large spring constant biases the configuration space by preventing the organic molecules from properly relaxing to accommodate short C−O distances. Here, we determine the value of the spring constant to be roughly 100−200 kcal/mol Å^2. The equilibrium C−O distance is found to be around 3 Å. Since the number of degrees of freedom corresponding to atoms in organic molecules is large, it is critical to capture proper initial configurations in z(I, II, and III) states to obtain a smooth MEP. We take the initial and final states for NEB calculations right before and after transition states during a small window of time (less than 100 fs) in biased MD simulations.[64,65] We find that the metastable intermediate complex (II), Figure 4, is stable for at least 20 ps in MD simulations at room temperature. Therefore, we divide the reaction path into two separate stages, one from state I to state II and the other from state II to state III; see states in Figure 2. Since the reaction does not directly involve water molecules, we do not include them in NEB calculations. This also helps with NEB's difficulty in determining the transition state in the presence of soft degrees of freedom. For the second stage of the chemical reaction, it is enough to elevate the temperature to 600 K to reach state III. To perform NEB calculations, we use the standard LAMMPS implementation of a two-stage NEB procedure.[86] First, we use the standard NEB[64] by constructing replicas with linear interpolation and imposing inter-replica forces to find the MEP. We subsequently use a barrier-climbing technique to find the true transition state.[65]

ASSOCIATED CONTENT

S **Supporting Information**

The Supporting Information is available free of charge on the ACS Publications website at DOI: 10.1021/acsnano.7b05815.

> TEM and SERS spectra from a control deposition, details on nanoparticle counting, TEM from a 20 nm Au nanosphere EHD-anhydride substrate, SEM of a 60 °C EHD-anhydride substrate after four deposition sequences, SEM from a 60 °C EHD-anhydride substrate highlighting PS-*b*-PMMA domains, SERS spectra dem-

onstrating intrasample uniformity, SERS spectra demonstrating sample stability in aqueous media (PDF)

AUTHOR INFORMATION

Corresponding Author
*E-mail: rragan@uci.edu.

ORCID
Allon I. Hochbaum: 0000-0002-5377-8065
Mohammad Javad Abdolhosseini Qomi: 0000-0001-6911-0994
Regina Ragan: 0000-0002-8694-5683

Notes
The authors declare no competing financial interest.

REFERENCES

(1) Murray, C. B.; Kagan, C. R.; Bawendi, M. G. Self-Organization of CdSe Nanocrystallites into Three-Dimensional Quantum Dot Superlattices. *Science* **1995**, *270*, 1335−1338.

(2) Gaulding, E. A.; Diroll, B. T.; Goodwin, E. D.; Vrtis, Z. J.; Kagan, C. R.; Murray, C. B. Deposition of Wafer-Scale Single-Component and Binary Nanocrystal Superlattice Thin Films *Via* Dip-Coating. *Adv. Mater.* **2015**, *27*, 2846−2851.

(3) Gong, J.; Newman, R. S.; Engel, M.; Zhao, M.; Bian, F.; Glotzer, S. C.; Tang, Z. Shape-Dependent Ordering of Gold Nanocrystals into Large-Scale Superlattices. *Nat. Commun.* **2017**, *8*, 14038.

(4) Vogel, N.; Retsch, M.; Fustin, C.-A; del Campo, A.; Jonas, U. Advances in Colloidal Assembly: The Design of Structure and Hierarchy in Two and Three Dimensions. *Chem. Rev.* **2015**, *115*, 6265−6311.

(5) Prodan, E.; Radloff, C.; Halas, N. J.; Nordlander, P. A Hybridization Model for the Plasmon Response of Complex Nanostructures. *Science* **2003**, *302*, 419−422.

(6) Ye, J.; Wen, F.; Sobhani, H.; Lassiter, J. B.; Dorpe, P. V.; Nordlander, P.; Halas, N. J. Plasmonic Nanoclusters: Near Field Properties of the Fano Resonance Interrogated with SERS. *Nano Lett.* **2012**, *12*, 1660−1667.

(7) Zhang, Y.; Wen, F.; Zhen, Y.-R.; Nordlander, P.; Halas, N. J. Coherent Fano Resonances in a Plasmonic Nanocluster Enhance Optical Four-Wave Mixing. *Proc. Natl. Acad. Sci. U. S. A.* **2013**, *110*, 921510.1073/pnas.1220304110.

(8) Campione, S.; Guclu, C.; Ragan, R.; Capolino, F. Fano Resonances in Metasurfaces Made of Linear Trimers of Plasmonic Nanoparticles. *Opt. Lett.* **2013**, *38*, 5216−5219.

(9) Campione, S.; Guclu, C.; Ragan, R.; Capolino, F. Enhanced Magnetic and Electric Fields *via* Fano Resonances in Metasurfaces of Circular Clusters of Plasmonic Nanoparticles. *ACS Photonics* **2014**, *1*, 254−260.

(10) Choi, J. H.; Adams, S. M.; Ragan, R. Design of a Versatile Chemical Assembly Method for Patterning Colloidal Nanoparticles. *Nanotechnology* **2009**, *20*, 065301.

(11) Adams, S. M.; Campione, S.; Caldwell, J. D.; Bezares, F. J.; Culbertson, J. C.; Capolino, F.; Ragan, R. Non-Lithographic SERS Substrates: Tailoring Surface Chemistry for Au Nanoparticle Cluster Assembly. *Small* **2012**, *8*, 2239−2249.

(12) Chen, W.; Tymchenko, M.; Gopalan, P.; Ye, X.; Wu, Y.; Zhang, M.; Murray, C. B.; Alu, A.; Kagan, C. R. Large-Area Nanoimprinted Colloidal Au Nanocrystal-Based Nanoantennas for Ultrathin Polarizing Plasmonic Metasurfaces. *Nano Lett.* **2015**, *15*, 5254−5260.

(13) Akselrod, G. M.; Huang, J.; Hoang, T. B.; Bowen, P. T.; Su, L.; Smith, D. R.; Mikkelsen, M. H. Large-Area Metasurface Perfect Absorbers from Visible to Near-Infrared. *Adv. Mater.* **2015**, *27*, 8028−8034.

(14) Hoang, T. B.; Akselrod, G. M.; Argyropoulos, C.; Huang, J.; Smith, D. R.; Mikkelsen, M. H. Ultrafast Spontaneous Emission Source Using Plasmonic Nanoantennas. *Nat. Commun.* **2015**, *6*, 7788.

(15) Kneipp, K.; Wang, Y.; Kneipp, H.; Perelman, L. T.; Itzkan, I.; Dasari, R. R.; Feld, M. S. Single Molecule Detection Using Surface-Enhanced Raman Scattering (SERS). *Phys. Rev. Lett.* **1997**, *78*, 1667−1670.

(16) Chikkaraddy, R.; de Nijs, B.; Benz, F.; Barrow, S. J.; Scherman, O. A.; Rosta, E.; Demetriadou, A.; Fox, P.; Hess, O.; Baumberg, J. J. Single-Molecule Strong Coupling at Room Temperature in Plasmonic Nanocavities. *Nature* **2016**, *535*, 127−130.

(17) Biswas, S.; Liu, X.; Jarrett, J. W.; Brown, D.; Pustovit, V.; Urbas, A.; Knappenberger, K. L.; Nealey, P. F.; Vaia, R. A. Nonlinear Chiro-Optical Amplification by Plasmonic Nanolens Arrays Formed *via* Directed Assembly of Gold Nanoparticles. *Nano Lett.* **2015**, *15*, 1836−1842.

(18) Hamon, C.; Liz-Marzán, L. M. Hierarchical Assembly of Plasmonic Nanoparticles. *Chem. - Eur. J.* **2015**, *21*, 9956−9963.

(19) Nam, J.-M.; Oh, J.-W.; Lee, H.; Suh, Y. D. Plasmonic Nanogap-Enhanced Raman Scattering with Nanoparticles. *Acc. Chem. Res.* **2016**, *49*, 2746−2755.

(20) Greybush, N. J.; Liberal, I.; Malassis, L.; Kikkawa, J. M.; Engheta, N.; Murray, C. B.; Kagan, C. R. Plasmon Resonances in Self-Assembled Two-Dimensional Au Nanocrystal Metamolecules. *ACS Nano* **2017**, *11*, 2917−2927.

(21) Flauraud, V.; Mastrangeli, M.; Bernasconi, G. D.; Butet, J.; Alexander, D. T. L.; Shahrabi, E.; Martin, O. J. F.; Brugger, J. Nanoscale Topographical Control of Capillary Assembly of Nanoparticles. *Nat. Nanotechnol.* **2017**, *12*, 73−80.

(22) Ni, S.; Klein, M. J. K.; Spencer, N. D.; Wolf, H. Cascaded Assembly of Complex Multiparticle Patterns. *Langmuir* **2014**, *30*, 90−95.

(23) Fleck, N. A.; McMeeking, R. M.; Kraus, T. Convective Assembly of a Particle Monolayer. *Langmuir* **2015**, *31*, 13655−13663.

(24) Ye, R.; Ye, Y.-H.; Zhou, Z.; Xu, H. Gravity-Assisted Convective Assembly of Centimeter-Sized Uniform Two-Dimensional Colloidal Crystals. *Langmuir* **2013**, *29*, 1796−1801.

(25) Jaquay, E.; Martínez, L. J.; Huang, N.; Mejia, C. A.; Sarkar, D.; Povinelli, M. L. Light-Assisted, Templated Self-Assembly of Gold Nanoparticle Chains. *Nano Lett.* **2014**, *14*, 5184−5188.

(26) Oberdick, S. D.; Majetich, S. A. Electrophoretic Deposition of Iron Oxide Nanoparticles on Templates. *J. Phys. Chem. C* **2013**, *117*, 18709−18718.

(27) Yilmaz, C.; Cetin, A. E.; Goutzamanidis, G.; Huang, J.; Somu, S.; Altug, H.; Wei, D.; Busnaina, A. Three-Dimensional Crystalline and Homogeneous Metallic Nanostructures Using Directed Assembly of Nanoparticles. *ACS Nano* **2014**, *8*, 4547−4558.

(28) Work, A. H.; Williams, S. J. Characterization of 2D Colloids Assembled by Optically-Induced Electrohydrodynamics. *Soft Matter* **2015**, *11*, 4266−4272.

(29) Wang, K.-C.; Kumar, A.; Williams, S. J.; Green, N. G.; Kim, K. C.; Chuang, H.-S. An Optoelectrokinetic Technique for Programmable Particle Manipulation and Bead-Based Biosignal Enhancement. *Lab Chip* **2014**, *14*, 3958−3967.

(30) Ristenpart, W. D.; Jiang, P.; Slowik, M. A.; Punckt, C.; Saville, D. A.; Aksay, I. A. Electrohydrodynamic Flow and Colloidal Patterning

near Inhomogeneities on Electrodes. *Langmuir* **2008**, *24*, 12172−12180.

(31) Mirkin, C. A.; Letsinger, R. L.; Mucic, R. C.; Storhoff, J. J. A DNA-Based Method for Rationally Assembling Nanoparticles into Macroscopic Materials. *Nature* **1996**, *382*, 607−609.

(32) Thacker, V. V.; Herrmann, L. O.; Sigle, D. O.; Zhang, T.; Liedl, T.; Baumberg, J. J.; Keyser, U. F. DNA Origami Based Assembly of Gold Nanoparticle Dimers for Surface-Enhanced Raman Scattering. *Nat. Commun.* **2014**, *5*.10.1038/ncomms4448

(33) Gür, F. N.; Schwarz, F. W.; Ye, J.; Diez, S.; Schmidt, T. L. Toward Self-Assembled Plasmonic Devices: High-Yield Arrangement of Gold Nanoparticles on DNA Origami Templates. *ACS Nano* **2016**, *10*, 5374−5382.

(34) Taylor, R. W.; Lee, T.-C.; Scherman, O. A.; Esteban, R.; Aizpurua, J.; Huang, F. M.; Baumberg, J. J.; Mahajan, S. Precise Subnanometer Plasmonic Junctions for SERS within Gold Nanoparticle Assemblies Using Cucurbit[n]uril "Glue. *ACS Nano* **2011**, *5*, 3878−3887.

(35) Sigle, D. O.; Kasera, S.; Herrmann, L. O.; Palma, A.; de Nijs, B.; Benz, F.; Mahajan, S.; Baumberg, J. J.; Scherman, O. A. Observing Single Molecules Complexing with Cucurbit[7]uril through Nanogap Surface-Enhanced Raman Spectroscopy. *J. Phys. Chem. Lett.* **2016**, *7*, 704−710.

(36) Van Haute, D.; Longmate, J. M.; Berlin, J. M. Controlled Assembly of Biocompatible Metallic Nanoaggregates Using a Small Molecule Crosslinker. *Adv. Mater.* **2015**, *27*, 5158−5164.

(37) Novak, J. P.; Feldheim, D. L. Assembly of Phenylacetylene-Bridged Silver and Gold Nanoparticle Arrays. *J. Am. Chem. Soc.* **2000**, *122*, 3979−3980.

(38) Sardar, R.; Heap, T. B.; Shumaker-Parry, J. S. Versatile Solid Phase Synthesis of Gold Nanoparticle Dimers Using an Asymmetric Functionalization Approach. *J. Am. Chem. Soc.* **2007**, *129*, 5356−5357.

(39) Zon, V. B.; Sachsenhauser, M.; Rant, U. Preparation of Gold Nanoparticle Dimers *via* Streptavidin-Induced Interlinking. *J. Nanopart. Res.* **2013**, *15*, 1−10.

(40) Kim, N. H.; Lee, S. J.; Moskovits, M. Reversible Tuning of SERS Hot Spots with Aptamers. *Adv. Mater.* **2011**, *23*, 4152−4156.

(41) Zhang, L.; Dai, L.; Rong, Y.; Liu, Z.; Tong, D.; Huang, Y.; Chen, T. Light-Triggered Reversible Self-Assembly of Gold Nanoparticle Oligomers for Tunable SERS. *Langmuir* **2015**, *31*, 1164−1171.

(42) Qian, X.; Li, J.; Nie, S. Stimuli-Responsive SERS Nanoparticles: Conformational Control of Plasmonic Coupling and Surface Raman Enhancement. *J. Am. Chem. Soc.* **2009**, *131*, 7540−7541.

(43) Zhu, M.-Q.; Wang, L.-Q.; Exarhos, G. J.; Li, A. D. Q. Thermosensitive Gold Nanoparticles. *J. Am. Chem. Soc.* **2004**, *126*, 2656−2657.

(44) Trau, M.; Saville, D. A.; Aksay, I. A. Assembly of Colloidal Crystals at Electrode Interfaces. *Langmuir* **1997**, *13*, 6375−6381.

(45) Squires, T. M.; Bazant, M. Z. Induced-Charge Electro-Osmosis. *J. Fluid Mech.* **1999**, *509*, 217−252.

(46) Saini, S.; Bukosky, S. C.; Ristenpart, W. D. Influence of Electrolyte Concentration on the Aggregation of Colloidal Particles near Electrodes in Oscillatory Fields. *Langmuir* **2016**, *32*, 4210−4216.

(47) Prieve, D. C.; Sides, P. J.; Wirth, C. L. 2-D Assembly of Colloidal Particles on a Planar Electrode. *Curr. Opin. Colloid Interface Sci.* **2010**, *15*, 160−174.

(48) Yan, Q.; Zheng, H.-N.; Jiang, C.; Li, K.; Xiao, S.-J. EDC/NHS Activation Mechanism of Polymethacrylic Acid: Anhydride *versus* NHS-Ester. *RSC Adv.* **2015**, *5*, 69939−69947.

(49) Kanipe, K. N.; Chidester, P. P. F.; Stucky, G. D.; Moskovits, M. Large Format Surface-Enhanced Raman Spectroscopy Substrate Optimized for Enhancement and Uniformity. *ACS Nano* **2016**, *10*, 7566−7571.

(50) Habermehl, A.; Liu, X.; Eschenbaum, C.; Lemmer, U. Fabrication of SERS Substrates by Roll-to-Roll Hot Embossing. In *Nano-Optics: Principles Enabling Basic Research and Applications*; *NATO Science for Peace and Security Series B: Physics and Biophysics*; Springer: Dordrecht, 2017; pp 513−515.

(51) Nakajima, N.; Ikada, Y. Mechanism of Amide Formation by Carbodiimide for Bioconjugation in Aqueous Media. *Bioconjugate Chem.* **1995**, *6*, 123−130.

(52) Solomentsev, Y.; Bevan, M.; Anderson, J. L. Aggregation Dynamics for Two Particles during Electrophoretic Deposition under Steady Fields. *Langmuir* **2000**, *16*, 9208−9216.

(53) Bell, W. C.; Booksh, K. S.; Myrick, M. L. Monitoring Anhydride and Acid Conversion in Supercritical/Hydrothermal Water by *in Situ* Fiber-Optic Raman Spectroscopy. *Anal. Chem.* **1998**, *70*, 332−339.

(54) Wu, G.; Van Alsenoy, C.; Geise, H. J.; Sluyts, E.; Van der Veken, B. J.; Shishkov, I. F.; Khristenko. Acetic Anhydride in the Gas Phase, Studied by Electron Diffraction and Infrared Spectroscopy, Supplemented With *Ab Initio* Calculations of Geometries and Force Fields. *J. Phys. Chem. A* **2000**, *104*, 1576−1587.

(55) Lucas, L. J.; Tellez, C.; Castilho, M. L.; Lee, C. L. D.; Hupman, M. A.; Vieira, L. S.; Ferreira, I.; Raniero, L.; Hewitt, K. C. Development of a Sensitive, Stable and EGFR-Specific Molecular Imaging Agent for Surface Enhanced Raman Spectroscopy. *J. Raman Spectrosc.* **2015**, *46*, 434−446.

(56) Bertie, J. E.; Michaelian, K. H. The Raman Spectrum of Gaseous Acetic Acid at 21 °C. *J. Chem. Phys.* **1982**, *77*, 5267−5271.

(57) Ito, K.; Bernstein, H. J. The Vibrational Spectra of the Formate, Acetate, and Oxalate Ions. *Can. J. Chem.* **1956**, *34*, 170−178.

(58) Saito, Y.; Machida, K. Vibrational Spectra and Structure of Acetylurea in the Crystalline State. *Spectrochim. Acta Part Mol. Spectrosc.* **1979**, *35*, 369−375.

(59) Marcus, M. A.; Lemley, A. T.; Lewis, A. Implications of Modelling the Chromophore of Rhodopsin and Bacteriorhodopsin with Resonance Raman Spectra of Retinal Schiff Bases. *J. Raman Spectrosc.* **1979**, *8*, 22−25.

(60) Frenkel, D.; Smit, B. *Understanding Molecular Simulation, Second ed.: From Algorithms to Applications*; Academic Press: San Diego, 2001.

(61) Monti, S.; Carravetta, V.; Ågren, H. Simulation of Gold Functionalization with Cysteine by Reactive Molecular Dynamics. *J. Phys. Chem. Lett.* **2016**, *7*, 272−276.

(62) van Duin, A. C. T.; Dasgupta, S.; Lorant, F.; Goddard, W. A. ReaxFF: A Reactive Force Field for Hydrocarbons. *J. Phys. Chem. A* **2001**, *105*, 9396−9409.

(63) Abad, J. M.; Mertens, S. F. L.; Pita, M.; Fernández, V. M.; Schiffrin, D. J. Functionalization of Thioctic Acid-Capped Gold Nanoparticles for Specific Immobilization of Histidine-Tagged Proteins. *J. Am. Chem. Soc.* **2005**, *127*, 5689−5694.

(64) Henkelman, G.; Jónsson, H. Improved Tangent Estimate in the Nudged Elastic Band Method for Finding Minimum Energy Paths and Saddle Points. *J. Chem. Phys.* **2000**, *113*, 9978−9985.

(65) Henkelman, G.; Uberuaga, B. P.; Jónsson, H. A Climbing Image Nudged Elastic Band Method for Finding Saddle Points and Minimum Energy Paths. *J. Chem. Phys.* **2000**, *113*, 9901−9904.

(66) Kennemur, J. G.; Novak, B. M. Advances in Polycarbodiimide Chemistry. *Polymer* **2011**, *52*, 1693−1710.

(67) Sides, P. J. Electrohydrodynamic Particle Aggregation on an Electrode Driven by an Alternating Electric Field Normal to It. *Langmuir* **2001**, *17*, 5791−5800.

(68) Russel, W. B.; Saville, D. A.; Schowalter, W. R. *Colloidal Dispersions*; Cambridge University Press, 1989.

(69) Wang, K.-C.; Kumar, A.; Williams, S.; Green, N.; Kim, K.; Chuang, H.-S. An Optoelectrokinetic Technique for Programmable Particle Manipulation and Bead-Based Biosignal Enhancement. *Lab Chip* **2014**, *14*, 3958−3967.

(70) Darvishzadeh-Varcheie, M.; Guclu, C.; Ragan, R.; Boyraz, O.; Capolino, F. Electric Field Enhancement with Plasmonic Colloidal Nanoantennas Excited by a Silicon Nitride Waveguide. *Opt. Express* **2016**, *24*, 28337−28352.

(71) Caldwell, J. D.; Glembocki, O.; Bezares, F. J.; Bassim, N. D.; Rendell, R. W.; Feygelson, M.; Ukaegbu, M.; Kasica, R.; Shirey, L.; Hosten, C. Plasmonic Nanopillar Arrays for Large-Area, High-Enhancement Surface-Enhanced Raman Scattering Sensors. *ACS Nano* **2011**, *5*, 4046−4055.

(72) Aggarwal, R. L.; Farrar, L. W.; Diebold, E. D.; Polla, D. L. Measurement of the Absolute Raman Scattering Cross Section of the 1584-cm−1 Band of Benzenethiol and the Surface-Enhanced Raman Scattering Cross Section Enhancement Factor for Femtosecond Laser-Nanostructured Substrates. *J. Raman Spectrosc.* **2009**, *40*, 1331−1333.

(73) Adams, S. M.; Campione, S.; Capolino, F.; Ragan, R. Directing Cluster Formation of Au Nanoparticles from Colloidal Solution. *Langmuir* **2013**, *29*, 4242−4251.

(74) Sam, S.; Touahir, L.; Salvador Andresa, J.; Allongue, P.; Chazalviel, J.-N.; Gouget-Laemmel, A. C.; Henry de Villeneuve, C.; Moraillon, A.; Ozanam, F.; Gabouze, N. S. Djebbar. Semiquantitative Study of the EDC/NHS Activation of Acid Terminal Groups at Modified Porous Silicon Surfaces. *Langmuir* **2010**, *26*, 809−814.

(75) Cai, W. B.; Ren, B.; Li, X. Q.; She, C. X.; Liu, F. M.; Cai, X. W.; Tian, Z. Q. Investigation of Surface-Enhanced Raman Scattering from Platinum Electrodes Using a Confocal Raman Microscope: Dependence of Surface Roughening Pretreatment. *Surf. Sci.* **1998**, *406*, 9−22.

(76) Grady, N. K.; Halas, N. J.; Nordlander, P. Influence of Dielectric Function Properties on the Optical Response of Plasmon Resonant Metallic Nanoparticles. *Chem. Phys. Lett.* **2004**, *399*, 167−171.

(77) Moerland, R. J.; Hoogenboom, J. P. Subnanometer-Accuracy Optical Distance Ruler Based on Fluorescence Quenching by Transparent Conductors. *Optica* **2016**, *3*, 112−117.

(78) Campione, S.; Adams, S. M.; Ragan, R.; Capolino, F. Comparison of Electric Field Enhancements: Linear and Triangular Oligomers *versus* Hexagonal Arrays of Plasmonic Nanospheres. *Opt. Express* **2013**, *21*, 7957−7973.

(79) Hanwell, M. D.; Curtis, D. E.; Lonie, D. C.; Vandermeersch, T.; Zurek, E.; Hutchison, G. R. Avogadro: An Advanced Semantic Chemical Editor, Visualization, and Analysis Platform. *J. Cheminf.* **2012**, *4*, 17.

(80) *Avogadro: an open-source molecular builder and visualization tool*, Version 1.1.1; https://avogadro.cc/cite/.

(81) Rappe, A. K.; Casewit, C. J.; Colwell, K. S.; Goddard, W. A.; Skiff, W. M. UFF, a Full Periodic Table Force Field for Molecular Mechanics and Molecular Dynamics Simulations. *J. Am. Chem. Soc.* **1992**, *114*, 10024−10035.

(82) Brenner, D. W. Empirical Potential for Hydrocarbons for Use in Simulating the Chemical Vapor Deposition of Diamond Films. *Phys. Rev. B: Condens. Matter Mater. Phys.* **1990**, *42*, 9458−9471.

(83) Tersoff, J. Empirical Interatomic Potential for Carbon, with Applications to Amorphous Carbon. *Phys. Rev. Lett.* **1988**, *61*, 2879−2882.

(84) Mortier, W. J.; Ghosh, S. K.; Shankar, S. Electronegativity-Equalization Method for the Calculation of Atomic Charges in Molecules. *J. Am. Chem. Soc.* **1986**, *108*, 4315−4320.

(85) Plimpton, S. Fast Parallel Algorithms for Short-Range Molecular Dynamics. *J. Comput. Phys.* **1995**, *117*, 1−19.

(86) Nakano, A. A Space−time-Ensemble Parallel Nudged Elastic Band Algorithm for Molecular Kinetics Simulation. *Comput. Phys. Commun.* **2008**, *178*, 280−289.